Tin Metal Improves the Lithiation Kinetics of High-Capacity Silicon Anodes

Kang Yao,[⊥] Na Li,[⊥] Ning Li, Eric Sivonxay, Yaping Du, Kristin A. Persson, Dong Su,* and Wei Tong*

ACCESS | Metrics & More | Article Recommendations | Supporting Information

ABSTRACT: Si-based anodes present a great promise for high energy density lithium-ion batteries. However, its commercialization is largely hindered by a grand challenge of a rapid capacity fade. Here, we demonstrate excellent cycling stability on a Si–Sn thin film electrode that outperforms pure Si or Sn counterpart under the similar conditions. Combined with the first-principles calculations, in situ transmission electron microscopy studies reveal a reduced volume expansion, increased conductivity, as well as dynamic rearrangement upon lithiation of the Si–Sn film. We attribute the improved lithiation kinetics to the formation of a conductive matrix that comprises a mosaic of nanostructured Sn, Li_ySn (specifically, Li_7Sn_2 develops around the lithiation potential of Si), and Li_xSi. This work provides an important advance in understanding the lithiation mechanism of Si-based anodes for next-generation lithium-ion batteries.
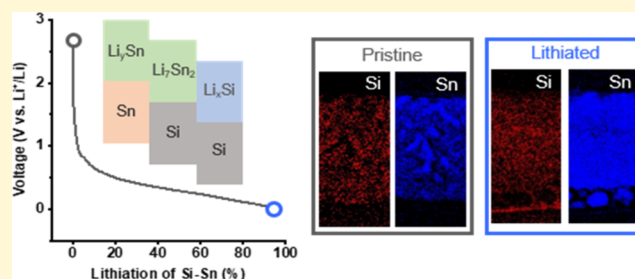
INTRODUCTION

Silicon is an attractive anode candidate for the next-generation lithium-ion batteries owing to its abundance and high theoretical capacity (4211 mA h g^{-1} for $Li_{4.4}Si$), which is more than 10 times that of the commercial graphite anode (372 mA h g^{-1}). It holds a great promise to meet the demands of portable electronics and electric vehicles for high energy density.[1−6] However, the significant drawback that hinders the widespread application of the Si anode is the rapid capacity decay upon electrochemical cycling.[7−9]

To improve the cycling stability of the high-capacity Si anode, material strategies have been employed by incorporating other elements, including active metals (Sn, Zn),[10−13] inactive metals (Ni, Fe, Mn),[14,15] or conductive C.[16,17] The major functionality of the additional element(s) is to provide a buffering matrix to accommodate the volume change upon (de)lithiation of Si. However, introducing inactive metals and/or carbon largely reduces the capacity of the Si anode. Of many active metal additives, Sn is of particular interest because of its electrochemical activity toward Li (theoretical capacity of 993 mA h g^{-1} for $Li_{4.4}Sn$), high electrical conductivity, and good ductility.[18,19] Because of the different physical properties, they exhibit varied electrochemical behaviors, for example, the Si anode typically starts with a crystalline phase and becomes amorphous upon cycling, while Sn is highly crystalline and its crystallinity remains during (de)lithiation.[20,21]

Combining active Si and Sn components has led to improved cycling stability at a reasonable capacity.[22−28] According to the phase diagram of Si–Sn, there is no miscibility between Si and Sn at low temperatures.[29] The electrochemical reaction of the X-ray amorphous Si–Sn thin film electrode was investigated by in situ X-ray diffraction (XRD), revealing two random local environments for Si and Sn (global amorphization) throughout the whole range of Li intercalation, with no X-ray crystalline phases as found in the Sn electrode.[30] In situ microscopic studies suggest a homogeneous and reversible volume change in the amorphous electrode, as opposed to the crystalline one.[31,32] The changes in atomic structure, elemental distribution, and morphology during electrochemical cycling are important factors for battery performance, especially in the Si electrode because its electrochemical reaction is rather dynamic, given its large volume change. A comprehensive understanding of these dynamic behaviors *in operando* for the tailored Si–Sn model electrode, showing consistent improvement, is essential to pursue effective directions for further advancement.

In this work, we employ in situ transmission electron microscopy (TEM) technique to investigate the lithiation processes of the Si and Si–Sn thin film electrodes for close comparison. The thin film electrodes that have similar configurations, free of binder/conductive carbon additive, and demonstrate the comparable electrochemistry to the composite electrodes lay the foundation for the mechanistic studies on the active materials themselves with no interference
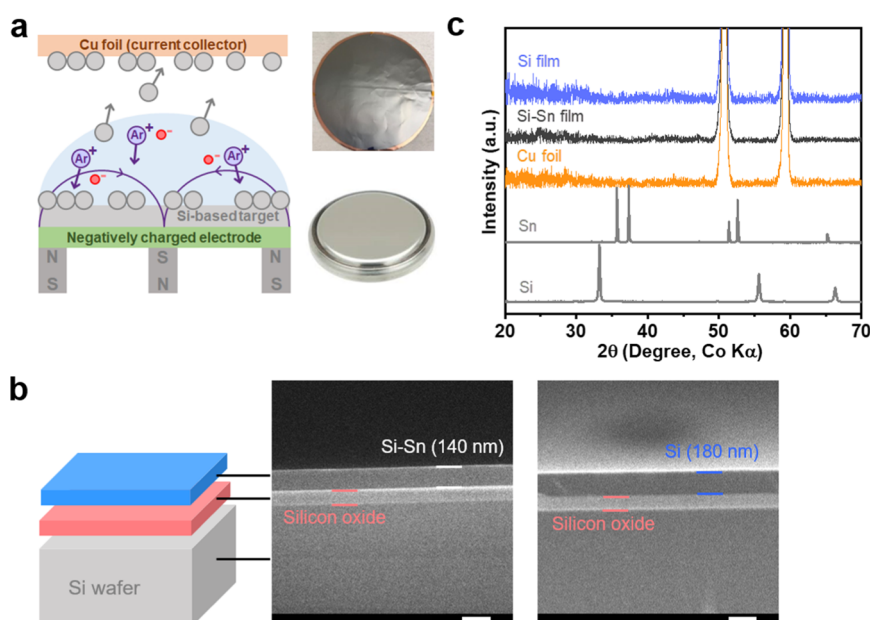
Figure 1. Synthesis and physical characterization of the Si-based thin film electrodes. (a) Integrated Si-based thin films deposited on the Cu foils directly used as the electrodes in the coin cells. (b) Cross-sectional SEM images of the Si−Sn and Si films along with a schematic, showing the films deposited on the Si wafer coated with 100 nm silicon oxide during the same run for thickness characterization. Scale bar is 200 nm. (c) XRD patterns of the Si and Si−Sn films along with Si, Sn, and Cu reference.

of other inactive components. The thicknesses and volume expansions of the electrode films are measured at different states of lithiation. We also investigate the phase evolution and elemental distribution during the lithiation of Si and Si−Sn thin film electrodes using selected area electron diffraction (SAED) and electron energy loss spectroscopy (EELS). Aided by the first-principles calculations, we propose a mosaic of mixed-conductive nanostructured matrix, which continuously evolves upon lithiation, facilitates the Li^+/e^- transport and induces a synergistic effect, accounting for the excellent cyclability of the Si−Sn electrode in comparison to the Si or Sn counterpart.

EXPERIMENTAL SECTION

Sample Preparation. 12 μm thick Cu foils are cleaned with acetone, isopropyl alcohol, and deionized water sequentially and then vacuum dried at 120 °C overnight. The treated Cu foils are fixed on 4 in. Si wafers for thin film deposition. Si, Si−Sn, and Sn films are deposited onto the Cu foils by direct current magnetron sputtering using a 3 in. p-type Si target (Kurt J. Lesker, 99.999% purity) and a 3 in. Sn target (Kurt J. Lesker, 99.998−99.999% purity). The base pressure is 2×10^{-5} Torr before deposition and 1.4×10^{-2} Torr during the deposition process. Films are also sputtered on the Si wafers coated with 100 nm thick silicon oxide during the same run to determine the film thickness. All the films are subsequently stored under vacuum to prevent air exposure.

Electrochemical Characterization. 2032-type Hohsen coin cells are assembled using the thin films deposited on Cu foils as the working electrodes (1.62 cm²), Li metal foil (99.9%, 0.75 mm thick, Thermo Scientific) as the counter electrodes, and 1 M $LiPF_6$ in ethylene carbonate−diethyl carbonate (50:50 w/w) as the electrolyte inside an Ar-filled glovebox. The cells are galvanostatically cycled between 1.5 and 0.01 V at C/20 based on the experimental capacity on a Maccor 4200 battery cycler at 30 °C. Cyclic voltammetry (CV) testing is carried out between 2 and 0.01 V at a scan rate of 0.1 mV/s using a VMP3 multichannel potentiostat (Bio-Logic Science Instruments). All the potential values are referenced to Li/Li^+.

Physical Characterization. XRD patterns are collected using a Bruker D8 Discover with Co Kα radiation (λ = 1.79 Å) operated at 35

kV/40 mA. Scanning electron microscopy (SEM) is performed on a JEOL JSM-7000F equipped with a Thermo Scientific energy-dispersive X-ray spectroscopy (EDS) detector. The cycled electrodes are harvested by disassembling the coin cells, rinsing with dimethyl carbonate, and natural drying inside the glovebox. Electrode samples are quickly transferred to the SEM chamber to study the morphological change after electrochemical cycling. The TEM samples are prepared by FEI Helios 600 dual beam focused ion beam (FIB) using the lift-out method. The in situ TEM electrochemical dry-cell is incorporated into a Nanofactory TEM−scanning tunneling microscopy specimen holder with detailed experiment setup described elsewhere.[33−35] The Li metal is coated onto a piezo-driven W probe as the counter electrode with a thin layer of Li_2O formed on the Li metal as the solid electrolyte. The Li electrode and FIB samples (Si and Si−Sn thin films) are loaded onto the holder inside an Ar-filled glovebox and then transferred to the TEM column using a sealed Ar bag to avoid the air exposure. The lithiation processes are captured in real time in either the TEM, SAED, or scanning TEM (STEM) mode on a JEOL 2100F TEM operated at 200 kV. The EELS mapping is conducted on a Hitachi HD2700C STEM with a probe aberration corrector.

First-Principles Calculations. We perform computational modeling to explore the dynamics of Li diffusion in amorphous Si, $Si_{0.62}Sn_{0.38}$, and Sn. These atomistic simulations are done using density functional theory and ab initio molecular dynamics (AIMD), as implemented in the Vienna ab initio simulation package.[36,37] To obtain amorphous structures, a liquid melt is generated following energy and density equilibration of a random arrangement of atoms, of at least 100 atoms following the desired stoichiometry, in a series of NVT AIMD simulations at 5000 K with a timestep of 2 fs. For diffusion calculations, three samples of the liquid melt are quenched to 500, 750, 1000, 1250, and 1500 K. Energy and density of each sample are equilibrated at each temperature before a final production run of 200 ps. For each temperature, diffusion coefficients are estimated as the slope of the diffusive regime within the hybrid ensemble/time-averaged mean square displacement, $\hat{b}_{hybrid}(t)$,[38] calculated as

$$\hat{b}_{hybrid}(t) = \frac{1}{NT} \sum_{k=1}^{N} \int_0^T [x^{(k)}(t' + t) - x^{(k)}(t')]^2 \, dt'$$
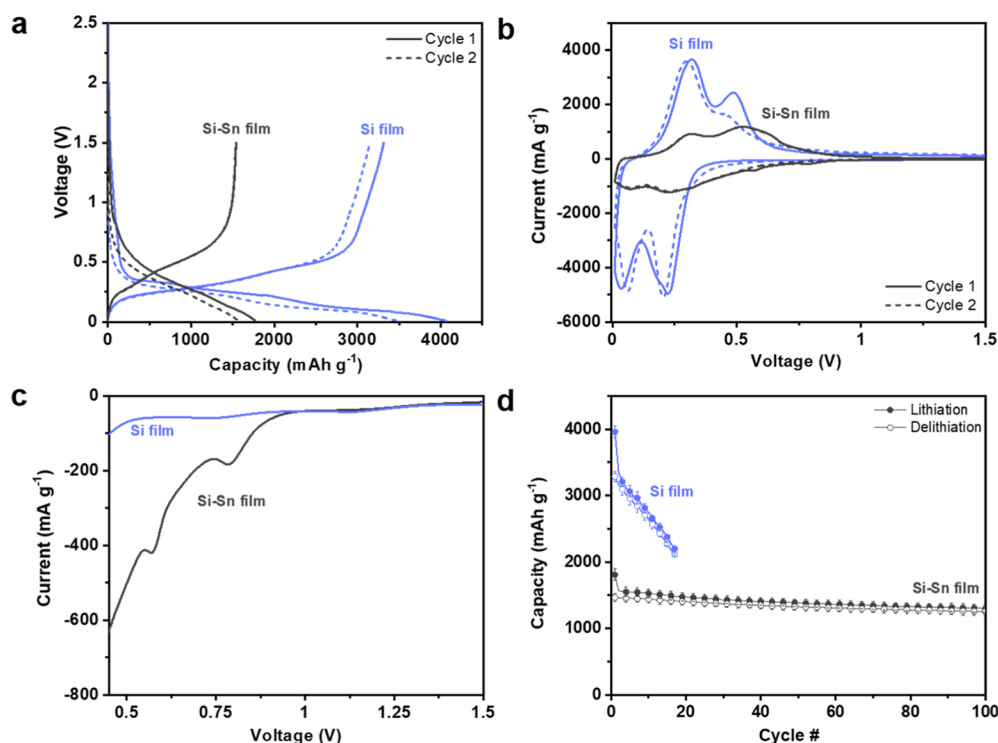
$$(1)$$

Figure 2. Electrochemistry of the Si-based thin film electrodes. (a) Charge−discharge profiles and (b) CV plots during the first two cycles; (c) CV plots enlarged in the range of 1.5−0.45 V during the first cycle, showing the lithiation of Sn occurs at a voltage higher than 0.45 V; and (d) cycling performance of the Si and Si−Sn film. Error bar shows the standard deviation calculated based on the capacity from triplicate cells.

where N is the number of sample trajectories, T is the simulation time of each trajectory, and x is the positions of the Li atoms. Room-temperature diffusion coefficients are extrapolated from non-linear regressions using the Arrhenius equation. Uncertainty on the extrapolated room temperature diffusivity (σ_D) is estimated, from the variance−covariance matrix for the regression, through the propagation of error, resulting in the below equation.

$$\sigma_D = \sqrt{\left(\frac{\sigma_{D_o} \times D}{D_o}\right)^2 + \left(\frac{\sigma_{E_A} \times D}{T}\right)^2} \tag{2}$$

where D is the diffusivity at temperature T and D_o is the pre-exponential factor. σ_{D_o} and σ_{EA} are the uncertainties in the pre-exponential factor and activation energy, respectively.

■ RESULTS AND DISCUSSION

Si-Based Thin Film Electrodes. Direct current magnetron sputtering system is used to deposit the Si-based thin films on Cu foils and both films show a similar morphology to Cu foil substrate (Figure S1). The as-produced films are directly used as electrodes in the coin cells for electrochemical characterization (Figure 1a). The composition of $Si_{0.62}Sn_{0.38}$, falling in the optimal composition range identified from previous work,[30,31] is selected and in good agreement with the EDS analysis. The thickness of the Si−Sn and Si films used for the detailed characterization is 140 and 180 nm, respectively (Figure 1b). Figure 1c shows the XRD patterns of the Si−Sn and Si films along with the references of Si, Sn, and Cu foil. Besides the characteristic peaks of Cu, no additional peaks from crystalline Si (c-Si) or crystalline Sn (c-Sn) are observed in the as-deposited thin films, suggesting that the films are amorphous.

The electrochemistry of the Si and Si−Sn thin film electrodes are presented in Figure 2. The a-Si film delivers initial lithiation and delithiation capacities of 4065 and 3317 mA h g^{-1}, respectively, while the Si−Sn film exhibits corresponding capacities of 1774 and 1540 mA h g^{-1} (Figure 2a). Note that the specific capacity reported here is calculated based on the mass obtained from the theoretical density, electrode thickness, and area because of the difficulty in measuring the actual weights of the films. With respect to the theoretical specific capacity of Si and Si−Sn, 4211 and 1887 mA h g^{-1}, respectively, both films achieve close to full lithiation (96.5 and 94.0% for the Si and Si−Sn, respectively). Details are presented in Table S1. The lithiation profile of the Si film is featured by two sloping plateaus around 0.3 and 0.1 V, consistent with the two-stage lithiation process of amorphous Si (a-Si).[2,39,40] The formation of the crystalline $Li_{15}Si_4$ (c-$Li_{15}Si_4$) is clearly suppressed in a-Si thin film, given the lack of a lithiation plateau around 0.45 V.[6,41] In comparison, the Si−Sn thin film displays a more continuous and sloping profile, with the (de)lithiation reaction starting at a higher voltage due to the presence of Sn (Figure S2a,b).[42] Correspondingly, the CV curves (Figure 2b,c) of the Si−Sn film are more steady, with less sharp lithiation/de lithiation peaks, compared to the a-Si film. The lithiation/delithiation processes of the Si−Sn film are more reversible and it displays better cycling stability than a-Si or Sn films (Figures 2d and S2c), with all being close to full lithiation. The Si−Sn film exhibits a capacity retention of 85.7% after 100 cycles. With no carbon additive or binder, we are motivated to scrutinize the underlying mechanism for the improved cyclability in the as-produced Si−Sn model electrode.

Volume Expansion Visualized by In Situ TEM. A significant challenge for the high-capacity anodes (i.e., Si and Sn) is poor capacity retention, which is strongly correlated with the massive volume change upon (de)lithiation. To
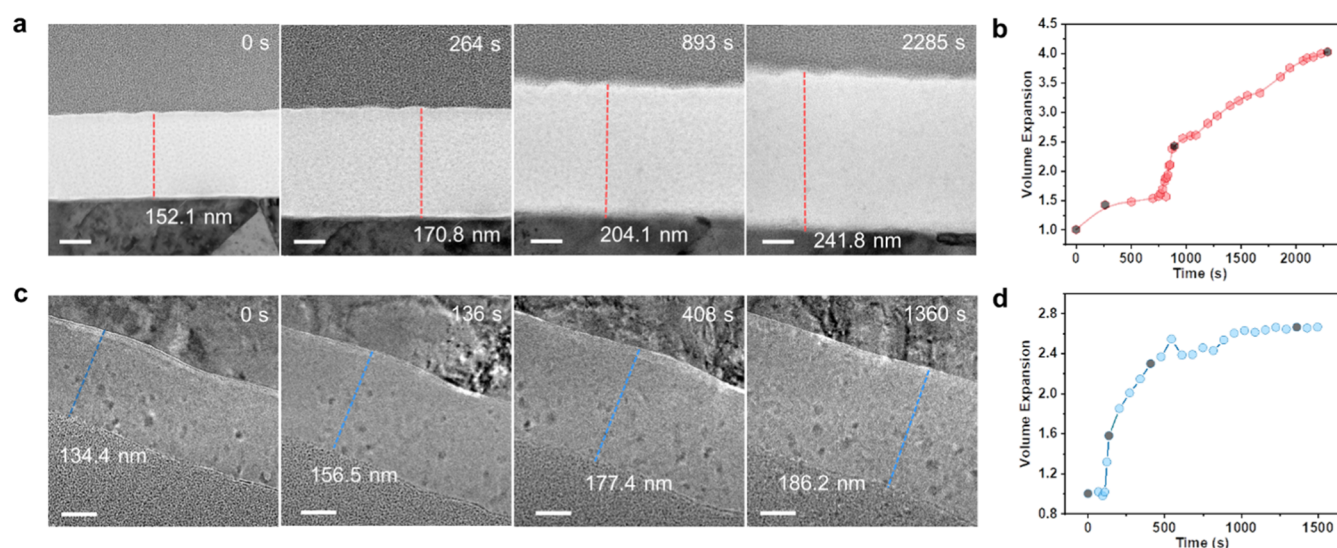
Figure 3. Volume expansion visualized by in situ TEM. (a) Cross-sectional in situ STEM images of the Si film and (c) cross-sectional in situ TEM images of the Si−Sn film captured at different time series, scale bar is 50 nm; volume expansion of the (b) Si film and (d) Si−Sn film calculated from corresponding in situ images upon lithiation. Black symbols in (b,d) mark the images captured in (a,c), respectively.

understand the distinct electrochemical behaviors between Si−Sn and Si, we first carried out in situ TEM study to visualize the morphological/structural change during the lithiation process. We note that there are no obvious pores revealed by TEM, though their presence is possible blow the resolution that can be achieved. A large thickness increase with reaction time is clearly visible for both Si−Sn (Figure 3a and Movie S1) and Si (Figure 3c and Movie S2), but the increase for the Si−Sn film is less pronounced. We plot the volume expansion with reaction time for each electrode (Figure 3b,d). Despite the expansion upon lithiation for both films, the magnitude of thickness change and the kinetics of the lithiation reaction are clearly different. For instance, the Si film shows an expansion of ∼400% of its original volume, much larger than that (266%) for Si−Sn after the full lithiation, assuming an equal expansion in all dimensions. The lower volume expansion for the Si−Sn film can be attributed to the flexible matrix and larger interstitial space of Sn that facilitates the accommodation of Li.[43]

With the smaller volume expansion upon lithiation of the Si−Sn film, we expect less cracking in the Si−Sn film. As revealed by SEM studies (Figure S3), the Si film cracks after the first cycle (Figure S3a,b), while the Si−Sn film remains intact after two cycles (Figure S3c,d). Accordingly, a gradual capacity fade is revealed for Si, but Si−Sn exhibits excellent cycling stability even after 100 cycles (Figure 2d) despite the noticeable cracking after the fifth cycle. Based on the observation of early film cracking and good cyclability of the Si−Sn film, it is inferred that cracking is not the only cause of the capacity decay for the Si anode.[1] Other factors (e.g., electrode conductivity), which could be induced by the electrode cracking, also contribute to the capacity fade.

Moreover, the lithiation process of Si is slow at the beginning (before ∼750 s), followed by faster lithiation later on (Figure 3b). In contrast, a fast reaction process is revealed for Si−Sn during the initial lithiation process (Figure 3d). It takes about half the time for Si−Sn to reach a similar level of expansion as Si, that is, for a volume expansion of 240%, it takes 893 s for Si compared to 408 s for Si−Sn. This can be explained by the different lithiation kinetics. a-Si lacks the long-

range ordering and consists of a continuous random network of Si atoms. At the beginning, the lithiation process of Si is limited by the Si−Si bond breaking. Upon further lithiation, the rate of Si−Si bond breakage gradually increases because the Li atoms nearby collectively weaken the Si−Si bond by electron transfer, and thus, the Li diffusivity increases. With the presence of Sn, the lithiation reaction initially starts with the alloying of Sn at a higher potential that occurs faster (Figure 3d) because of the greater Li diffusivity in Sn, about 2 orders of magnitude higher than Si (Figure 4). The presence of Sn, though immiscible, suppresses the volume expansion and modifies the kinetics of the lithiation process.
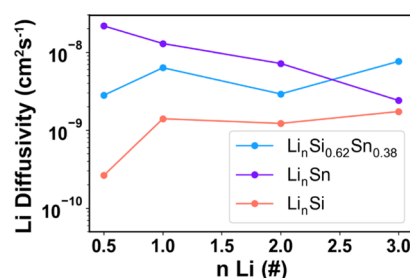

Figure 4. Li ion diffusivity derived from the first-principles calculations. Calculated Li^+ diffusivity in a-Sn and a-$Si_{0.62}Sn_{0.38}$ is much higher than that in a-Si.

Phase Evolution Tracked by In Situ SAED. The phase evolution of the Si and Si−Sn films during lithiation is probed via in situ SAED (Figure 5 and Movies S3 and S4) from a selected area of 150 nm. Before lithiation, the SAED pattern of Si (Figure 5a) consists of the broad diffuse rings with no bright spots related to c-Si phase, confirming its amorphous feature, while the Si−Sn film displays nanocrystallinity (Figure 5e), though it is not detectable by XRD due to the lack of long-range ordering (Figure S4a,c). After full lithiation, a-Si phase transforms to amorphous $Li_{22}Si_5$ (Figures 5b and S4b), in comparison to amorphous $Li_{22}Si_5$ and crystalline $Li_{22}Sn_5$ phases after lithiation of Si−Sn [Figures 5f and S4d and SAED pattern (2093 s) in Figure S5]. A trace amount of
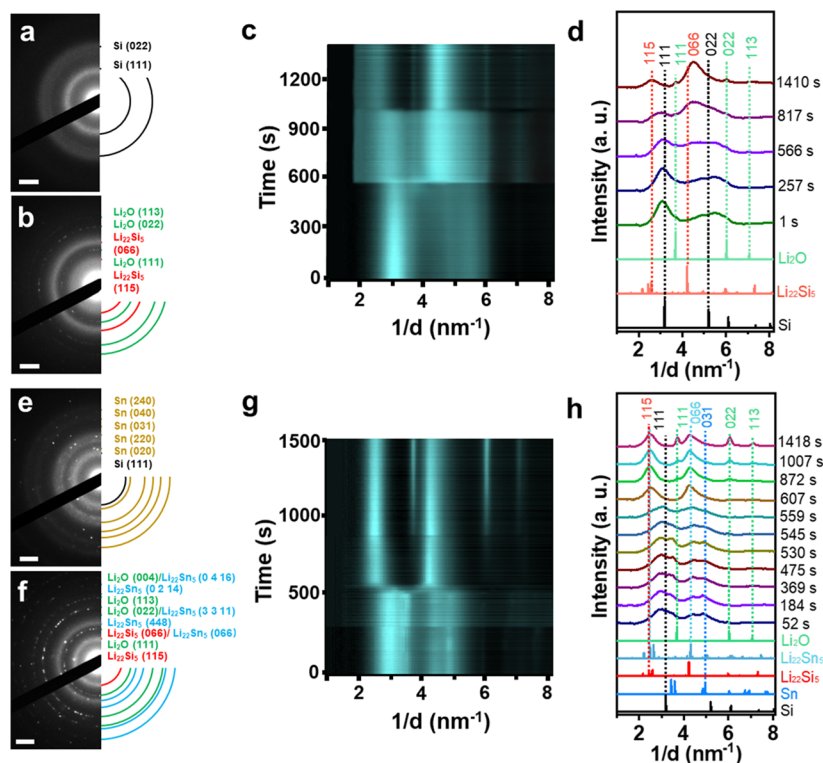
Figure 5. Phase evolution tracked by in situ SAED. SAED patterns of (a) pristine Si film, (b) fully lithiated Si film, (e) pristine Si–Sn film, and (f) fully lithiated Si–Sn film, scale bar is 2 1/nm. Electron diffraction intensity profiles as a function of reaction time during the in situ lithiation of (c) Si and (g) Si–Sn films. Integrated intensity profiles of (d) Si in time sequence along with Si, $Li_{22}Si_5$, and Li_2O reference and (h) Si–Sn along with Si, Sn, $Li_{22}Si_5$, $Li_{22}Sn_5$, and Li_2O reference.
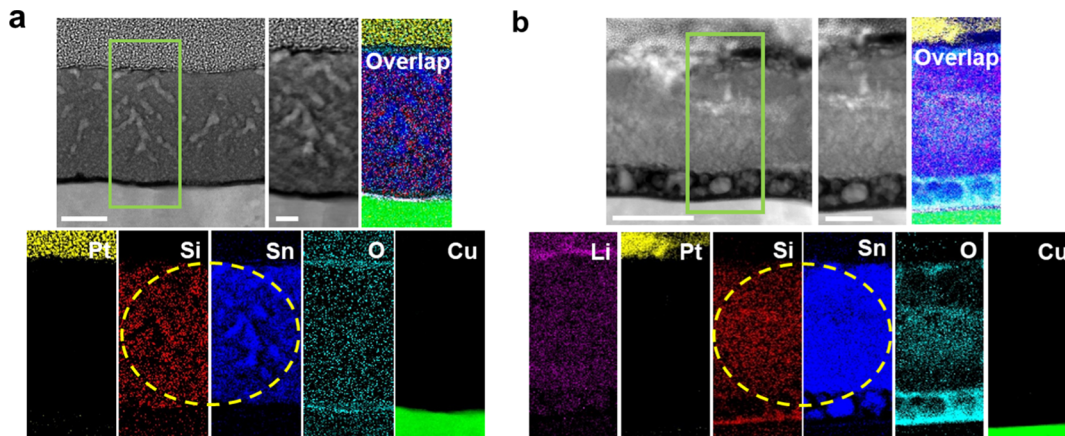

Figure 6. Dynamic elemental rearrangement during the lithiation of Si–Sn mapped by EELS. Microstructure and elemental distribution at (a) pristine and (b) fully lithiated states for the Si–Sn film. Scale bar from left to right is 50, 20 nm in (a) and 100, 50 nm in (b).

crystalline Li_2O is revealed in both cases due to the presence of surface oxide (Figures 5d,h and S5).

To track the phase evolution, the electron diffraction intensity profiles as a function of reaction time during in situ lithiation are plotted in Figure 5c (Si) and Figure 5g (Si–Sn), and the integrated intensity profiles from a series of time-sequenced SAED patterns are shown in Figure 5d (Si) and Figure 5h (Si–Sn). For Si, the two-phase change starts around 550 s and becomes clearly visible around 1000 s, as evidenced by the diminishing Si(111) peak and the emerging $Li_{22}Si_5$ (115) and (066) peaks as the reaction proceeds. The lithiation reaction of Si–Sn is featured by the evolution of a series of intermediate Li_ySn and Li_xSi phases [SAED patterns (549–580

s) in Figure S5]. The intensity profiles suggest a major phase change occurring around 550 s, consistent with the reaction-rate-changing step in Figure 5d. Before ~550 s, the Sn phase readily reacts, and the intensity of the Sn(031) peak declines with the reaction time. Along with the Li_7Sn_2 phase, the Li_xSi phase is captured in sequence within a few tens of seconds (Figure S5). By 580 s, the Li-rich $Li_{13}Si_4$ phase forms. Starting at 607 s (Figure 5h), the significant peak shifts to $Li_{22}Sn_5$ and $Li_{22}Si_5$ in the intensity profiles correspond to the slow-reaction-rate region in Figure 3d.

These results indicate that the two immiscible components in the Si–Sn thin film electrode undergo consecutive lithiation, with conductive Sn reacting first. From the in situ SAED

analysis of the Si—Sn film, we observe the formation of the Li_7Sn_2 phase around the initiation of Si lithiation [SAED pattern (554 s) in Figure S5], which is supposed to develop around the electrochemical potential of Si lithiation.[18,20] The formation of Li_7Sn_2 phase may substantially accelerate the Si—Si bond breaking and enhance the Li diffusivity, therefore modifying the lithiation reaction kinetics.

Dynamic Elemental Rearrangement upon Lithiation of Si—Sn Mapped by EELS. The EELS maps are also collected to investigate the elemental distribution before and after the lithiation reaction (Figure 6). The EELS maps were collected on the exactly same area at the nanoscale before and after lithiation. Before lithiation, the Si—Sn film displays a morphology of branch-like networks (Figure 6a). The separation between Si and Sn occurs at the nanometer scale, which is ascribed to the strong propensity of ductile Sn to segregate and crystallize. This is commensurate with the phase diagram of Si—Sn, showing no miscibility between Si and Sn at low temperatures.[29] Interestingly, such branch-like morphology disappears, and instead, a uniform distribution of Si and Sn is observed after lithiation (Figure 6b). This dynamic elemental rearrangement should be correlated with the bond breaking.[44,45] Consistent with the nanosecond-scale simulations on a-Si, stating the host is not static but undergoes a rearrangement from isolated atoms to chains and clusters,[46] we reveal a similar dynamic behavior upon lithiation of Si—Sn. More importantly, this dynamic process ultimately leads to a uniform elemental distribution between the two components that are prone to separate at the pristine state. This finding implies that the elemental homogeneity at the pristine state is not an indispensable physical property toward the development of the high-capacity Si anode because it can be self-healed upon lithiation at the nanometer scale. Instead, other properties such as the mobility of the incorporated elements and Li diffusivity in the lithiated phases are of critical importance because the intermediate lithiation products can manipulate the lithiation process and favorably drive the electrochemical reaction.

We have shown that a Si—Sn thin film electrode with no conductive carbon, binder, or electrolyte additive (i.e., fluoroethylene carbonate) exhibits stable cycling, which outperforms its Si or Sn counterpart and lays the foundation to investigate the underlying lithiation mechanism. From the in situ TEM/STEM imaging, we visualize a reduced volume expansion of Si—Sn compared to Si. At the early stage of lithiation, the Sn phase in the composite reacts with Li and expands in the presence of the unreacted Si phase, serving as a matrix to buffer the expansion of the reacted Sn phases. In this regard, the mutual buffering effect is expected to preserve the dimensional integrity and microstructure of the Si—Sn electrode.

On the other hand, Si—Sn exhibits a faster reaction kinetics than Si. The excellent cycling behavior of Si—Sn is attributed to the in situ formation of mixed (e^- and Li^+) conducting matrix, in which the reactants are finely dispersed. Sn has a high electrical conductivity of 9.2×10^4 S cm^{-1} at 20 °C, 9 orders of magnitude higher than Si. Electrically conductive Sn along with ionically conductive lithiated Sn/Si (Li_ySn and Li_xSi) phases constitute the solid mixed-conductive matrix for Si. Such electrical and ionic integrity in the Si—Sn electrode, despite the microcracking, is the key to achieve excellent cycling stability. Based on the experimental observations, we propose the reaction mechanism for the Si—Sn electrode

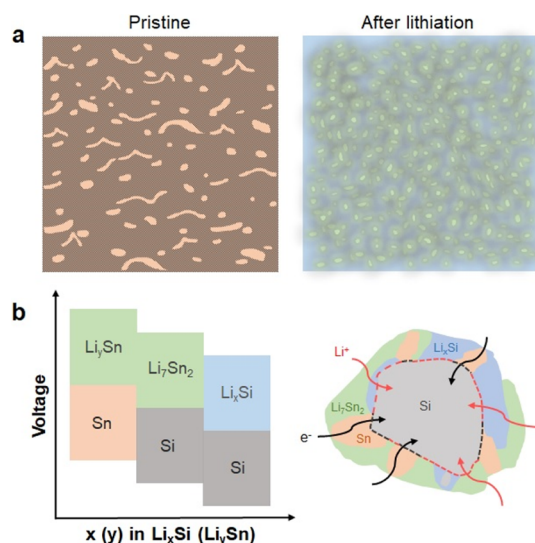(Figure 7). The microstructure of the Si—Sn thin film electrode changes from a phase-separated branch-like

Figure 7. Schematic of lithiation mechanism for the Si—Sn electrode. (a) Microstructural evolution originating from the volume expansion upon lithiation leads to homogeneous elemental distribution and (b) Sn, Li_xSi, and Li_ySn facilitate mixed conductive matrix and promote the lithiation kinetics.

morphology (seemingly unfavored physical character) to the homogeneous elemental distribution after lithiation (Figure 7a). Such elemental redistribution builds a mosaic of nanostructured Si, Sn, Li_ySn, and Li_xSi phases that continuously evolves and redistributes so that Si is surrounded by electrically conductive Sn and ionically conductive Li_ySn/Li_xSi (Figure 7b). Although the electrochemistry of thin film electrodes could differ from that of the composite ones, the knowledge gained here should provide additional insights into the fundamental understanding of silicon anode behavior, particularly, the role of Sn in improving electrical and ionic conductivity as well as electrode integrity. In principle, such a beneficial effect can be harnessed if a homogeneous mixing between Si and Sn is achieved at the nanometer scale.

■ CONCLUSIONS

In summary, the in situ characterization at the nanoscale reveals the incorporation of Sn essentially modifies the lithiation mechanism. A smaller volume expansion upon lithiation of Si—Sn than Si is revealed, which delays but does not eliminate the electrode cracking, suggesting electrode cracking is a secondary factor for capacity fade. Instead, the presence of Sn essentially maintains the overall electrical and ionic conductivity integrity in the electrode owing to its intrinsically high electrical conductivity and ionic conductivity of the in situ formed lithiated phases, especially which forms around the electrochemical potential for the lithiation reaction of Si, ultimately resulting in a synergy between the immiscible Si and Sn. These electrochemically favored behaviors are further promoted when the elemental redistribution occurs during the lithiation process. This work provides an in-depth understanding of the improved performance through the integration of additional elements for the development of high-energy Si-based anodes.

■ ASSOCIATED CONTENT

ⓢ Supporting Information

The Supporting Information is available free of charge at https://pubs.acs.org/doi/10.1021/acs.chemmater.2c01867.

SEM and HR-TEM images of Si and Si−Sn films at different states of charge, physical and electrochemical properties of Si and Si−Sn films during the first cycle, electrochemistry of the Sn film, and SAED analysis of the Si−Sn film during lithiation (PDF)

In situ STEM observation of the lithiation process of the pure Si film (MOV)

In situ TEM observation of the lithiation process of the Si−Sn film (MOV)

In situ SAED observation of the lithiation process of the pure Si film (MOV)

In situ SAED observation of the lithiation process of the Si-Sn film (MOV)

■ AUTHOR INFORMATION

Corresponding Authors

Dong Su − *Center for Functional Nanomaterials, Brookhaven National Laboratory, Upton, New York 11973, United States*; Email: free.sd@gmail.com

Wei Tong − *Energy Storage and Distributed Resources Division, Lawrence Berkeley National Laboratory, Berkeley, California 94720, United States*; ⓞ orcid.org/0000-0002-2878-1297; Email: weitong@lbl.gov

Authors

Kang Yao − *Energy Storage and Distributed Resources Division, Lawrence Berkeley National Laboratory, Berkeley, California 94720, United States*; ⓞ orcid.org/0000-0002-4540-7811

Na Li − *Center for Functional Nanomaterials, Brookhaven National Laboratory, Upton, New York 11973, United States; School of Materials Science and Engineering & National Institute for Advanced Materials, Nankai University, Tianjin 300350, China*

Ning Li − *Energy Storage and Distributed Resources Division, Lawrence Berkeley National Laboratory, Berkeley, California 94720, United States*; ⓞ orcid.org/0000-0002-1830-2723

Eric Sivonxay − *Department of Materials Science and Engineering, University of California, Berkeley, Berkeley, California 94720, United States*

Yaping Du − *School of Materials Science and Engineering & National Institute for Advanced Materials, Nankai University, Tianjin 300350, China*; ⓞ orcid.org/0000-0002-9937-2087

Kristin A. Persson − *Energy Storage and Distributed Resources Division, Lawrence Berkeley National Laboratory, Berkeley, California 94720, United States; Department of Materials Science and Engineering, University of California, Berkeley, Berkeley, California 94720, United States*; ⓞ orcid.org/0000-0003-2495-5509

Complete contact information is available at:
https://pubs.acs.org/10.1021/acs.chemmater.2c01867

Author Contributions

[⊥]K.Y. and N.L. contributed equally.

Notes

The authors declare no competing financial interest.

■ ACKNOWLEDGMENTS

■ REFERENCES

(1) Maranchi, J. P.; Hepp, A. F.; Kumta, P. N. High Capacity, Reversible Silicon Thin-Film Anodes for Lithium-Ion Batteries. *Electrochem. Solid-State Lett.* **2003**, *6*, A198.

(2) Obrovac, M. N.; Krause, L. J. Reversible Cycling of Crystalline Silicon Powder. *J. Electrochem. Soc.* **2007**, *154*, A103−A108.

(3) Chan, C. K.; Peng, H. L.; Liu, G.; McIlwrath, K.; Zhang, X. F.; Huggins, R. A.; Cui, Y. High-Performance Lithium Battery Anodes Using Silicon Nanowires. *Nat. Nanotechnol.* **2008**, *3*, 31−35.

(4) Chan, C. K.; Patel, R. N.; O'Connell, M. J.; Korgel, B. A.; Cui, Y. Solution-Grown Silicon Nanowires for Lithium-Ion Battery Anodes. *ACS Nano* **2010**, *4*, 1443−1450.

(5) Wu, H.; Chan, G.; Choi, J. W.; Ryu, I.; Yao, Y.; McDowell, M. T.; Lee, S. W.; Jackson, A.; Yang, Y.; Hu, L. B.; Cui, Y. Stable Cycling of Double-Walled Silicon Nanotube Battery Anodes Through Solid-Electrolyte Interphase Control. *Nat. Nanotechnol.* **2012**, *7*, 310−315.

(6) Obrovac, M.; Chevrier, V. Alloy Negative Electrodes for Li-Ion Batteries. *Chem. Rev.* **2014**, *114*, 11444−11502.

(7) Kasavajjula, U.; Wang, C.; Appleby, A. J. Nano- and Bulk-Silicon-Based Insertion Anodes for Lithium-Ion Secondary Cells. *J. Power Sources* **2007**, *163*, 1003−1039.

(8) Szczech, J. R.; Jin, S. Nanostructured Silicon for High Capacity Lithium Battery Anodes. *Energy Environ. Sci.* **2011**, *4*, 56−72.

(9) Liu, X. H.; Zhong, L.; Huang, S.; Mao, S. X.; Zhu, T.; Huang, J. Y. Size-Dependent Fracture of Silicon Nanoparticles During Lithiation. *ACS Nano* **2012**, *6*, 1522−1531.

(10) Hatchard, T.; Dahn, J. Study of the Electrochemical Performance of Sputtered $Si_{1-x}Sn_x$ Films. *J. Electrochem. Soc.* **2004**, *151*, A1628−A1635.

(11) Hatchard, T.; Obrovac, M.; Dahn, J. Electrochemical Reaction of the $Si_{1-x}Zn_x$ Binary System with Li. *J. Electrochem. Soc.* **2005**, *152*, A2335−A2344.

(12) Al-Maghrabi, M.; Thorne, J.; Sanderson, R.; Byers, J.; Dahn, J.; Dunlap, R. A Combinatorial Study of the Sn-Si-C System for Li-Ion Battery Applications. *J. Electrochem. Soc.* **2012**, *159*, A711−A719.

(13) Xiao, X.; Wang, J. S.; Liu, P.; Sachdev, A. K.; Verbrugge, M. W.; Haddad, D.; Balogh, M. P. Phase-Separated Silicon−Tin Nanocomposites for High Capacity Negative Electrodes in Lithium Ion Batteries. *J. Power Sources* **2012**, *214*, 258−265.

(14) Fleischauer, M.; Topple, J.; Dahn, J. Combinatorial Investigations of Si-M (M = Cr + Ni, Fe, Mn) Thin Film Negative Electrode Materials. *Electrochem. Solid-State Lett.* **2005**, *8*, A137−A140.

(15) Cao, Y.; Bennett, J. C.; Dunlap, R. A.; Obrovac, M. N. Li Insertion in Ball Milled Si-Mn Alloys. *J. Electrochem. Soc.* **2018**, *165*, A1734−A1740.

(16) Magasinski, A.; Dixon, P.; Hertzberg, B.; Kvit, A.; Ayala, J.; Yushin, G. High-Performance Lithium-Ion Anodes Using a Hierarchical Bottom-Up Approach. *Nat. Mater.* **2010**, *9*, 353−358.

(17) Lee, J. K.; Smith, K. B.; Hayner, C. M.; Kung, H. H. Silicon Nanoparticles−Graphene Paper Composites for Li Ion Battery Anodes. *Chem. Commun.* **2010**, *46*, 2025−2027.

(18) Yang, S.; Zavalij, P. Y.; Whittingham, M. S. Anodes for Lithium Batteries: Tin Revisited. *Electrochem. Commun.* **2003**, *5*, 587−590.

(19) Ying, H.; Han, W.-Q. Metallic Sn-Based Anode Materials: Application in High-Performance Lithium-Ion and Sodium-Ion Batteries. *Adv. Sci.* **2017**, *4*, 1700298.

(20) Wang, J.; Fan, F.; Liu, Y.; Jungjohann, K. L.; Lee, S. W.; Mao, S. X.; Liu, X.; Zhu, T. Structural Structural Evolution and Pulverization of Tin Nanoparticles during Lithiation-Delithiation Cycling. *J. Electrochem. Soc.* **2014**, *161*, F3019−F3024.

(21) Li, Q.; Wang, P.; Feng, Q.; Mao, M.; Liu, J.; Mao, S. X.; Wang, H. In Situ TEM on the Reversibility of Nanosized Sn Anodes during the Electrochemical Reaction. *Chem. Mater.* **2014**, *26*, 4102−4108.

(22) Chockla, A. M.; Klavetter, K. C.; Mullins, C. B.; Korgel, B. A. Tin-Seeded Silicon Nanowires for High Capacity Li-Ion Batteries. *Chem. Mater.* **2012**, *24*, 3738−3745.

(23) Wang, H.; Huang, H.; Chen, L.; Wang, C.; Yan, B.; Yu, Y.; Yang, Y.; Yang, G. Preparation of Si/Sn-Based Nanoparticles Composited with Carbon Fibers and Improved Electrochemical Performance as Anode Materials. *ACS Sustainable Chem. Eng.* **2014**, *2*, 2310−2317.

(24) Kawasaki, M.; Laokawee, V.; Sarakonsri, T.; Hashizume, T.; Shiojiri, M. Structural Investigation Of Sisn/(Reduced Graphene Oxide) Nanocomposite Powder for Li-Ion Battery Anode Applications. *J. Appl. Phys.* **2016**, *120*, 204302.

(25) Whiteley, J. M.; Kim, J. W.; Piper, D. M.; Lee, S.-H. High-Capacity and Highly Reversible Silicon-Tin Hybrid Anode for Solid-State Lithium-Ion Batteries. *J. Electrochem. Soc.* **2016**, *163*, A251−A254.

(26) Jin, Y.; Tan, Y.; Hu, X.; Zhu, B.; Zheng, Q.; Zhang, Z.; Zhu, G.; Yu, Q.; Jin, Z.; Zhu, J. Scalable Production of the Silicon−Tin Yin-Yang Hybrid Structure with Graphene Coating for High Performance Lithium-Ion Battery Anodes. *ACS Appl. Mater. Interfaces* **2017**, *9*, 15388−15393.

(27) Xu, J.; Ling, M.; Terborg, L.; Zhao, H.; Qiu, F.; Urban, J. J.; Kostecki, R.; Liu, G.; Tong, W. Facile Synthesis and Electrochemistry of Si-Sn-C Nanocomposites for High-Energy Li-Ion Batteries. *J. Electrochem. Soc.* **2017**, *164*, A1378−A1383.

(28) Yao, K.; Ling, M.; Liu, G.; Tong, W. Chemical Reduction Synthesis and Electrochemistry of Si−Sn Nanocomposites as High-Capacity Anodes for Li-Ion Batteries. *J. Phys. Chem. Lett.* **2018**, *9*, 5130−5134.

(29) Olesinski, R. W.; Abbaschian, G. J. The Si−Sn (Silicon−Tin) System. *Bull. Alloy Phase Diagrams* **1984**, *5*, 273−276.

(30) Beaulieu, L.; Hewitt, K.; Turner, R.; Bonakdarpour, A.; Abdo, A.; Christensen, L.; Eberman, K.; Krause, L.; Dahn, J. The Electrochemical Reaction of Li with Amorphous Si-Sn Alloys. *J. Electrochem. Soc.* **2003**, *150*, A149−A156.

(31) Beaulieu, L.; Hatchard, T.; Bonakdarpour, A.; Fleischauer, M.; Dahn, J. Reaction of Li with Alloy Thin Films Studied by In Situ AFM. *J. Electrochem. Soc.* **2003**, *150*, A1457−A1464.

(32) Timmons, A.; Dahn, J. R. In Situ Optical Observations of Particle Motion in Alloy Negative Electrodes for Li-Ion Batteries. *J. Electrochem. Soc.* **2006**, *153*, A1206−A1210.

(33) Hwang, S.; Meng, Q.; Chen, P. F.; Kisslinger, K.; Cen, J.; Orlov, A.; Zhu, Y.; Stach, E. A.; Chu, Y. H.; Su, D. Strain Coupling of Conversion−Type Fe_3O_4 Thin Films for Lithium Ion Batteries. *Angew. Chem., Int. Ed.* **2017**, *56*, 7813−7816.

(34) He, K.; Zhang, S.; Li, J.; Yu, X.; Meng, Q.; Zhu, Y.; Hu, E.; Sun, K.; Yun, H.; Yang, X.-Q. Visualizing Non-Equilibrium Lithiation of Spinel Oxide via In Situ Transmission Electron Microscopy. *Nat. Commun.* **2016**, *7*, 11441.

(35) Huang, J. Y.; Zhong, L.; Wang, C. M.; Sullivan, J. P.; Xu, W.; Zhang, L. Q.; Mao, S. X.; Hudak, N. S.; Liu, X. H.; Subramanian, A. In Situ Observation of The Electrochemical Lithiation of a Single SnO_2 Nanowire Electrode. *Science* **2010**, *330*, 1515−1520.

(36) Kresse, G.; Furthmüller, J. Efficiency of Ab-Initio Total Energy Calculations for Metals and Semiconductors Using a Plane-Wave Basis Set. *Comput. Mater. Sci.* **1996**, *6*, 15−50.

(37) Kresse, G.; Furthmüller, J. Efficient Iterative Schemes for Ab Initio Total-Energy Calculations Using a Plane-Wave Basis Set. *Phys. Rev. B: Condens. Matter Mater. Phys.* **1996**, *54*, 11169−11186.

(38) Kim, C.; Borodin, O.; Karniadakis, G. E. Quantification of Sampling Uncertainty for Molecular Dynamics Simulation: Time-Dependent Diffusion Coefficient in Simple Fluids. *J. Comput. Phys.* **2015**, *302*, 485−508.

(39) Wang, J. W.; He, Y.; Fan, F.; Liu, X. H.; Xia, S.; Liu, Y.; Harris, C. T.; Li, H.; Huang, J. Y.; Mao, S. X. Two-Phase Electrochemical Lithiation in Amorphous Silicon. *Nano Lett.* **2013**, *13*, 709−715.

(40) McDowell, M. T.; Lee, S. W.; Harris, J. T.; Korgel, B. A.; Wang, C.; Nix, W. D.; Cui, Y. In Situ TEM of Two-Phase Lithiation of Amorphous Silicon Nanospheres. *Nano Lett.* **2013**, *13*, 758−764.

(41) Iwamura, S.; Nishihara, H.; Kyotani, T. Fast and Reversible Lithium Storage in a Wrinkled Structure Formed from Si Nanoparticles During Lithiation/Delithiation Cycling. *J. Power Sources* **2013**, *222*, 400−409.

(42) Boukamp, B.; Lesh, G.; Huggins, R. All-Solid Lithium Electrodes with Mixed-Conductor Matrix. *J. Electrochem. Soc.* **1981**, *128*, 725−729.

(43) Chou, C.-Y.; Kim, H.; Hwang, G. S. A Comparative First-Principles Study of the Structure, Energetics, and Properties Of Li−M (M= Si, Ge, Sn) Alloys. *J. Phys. Chem. C* **2011**, *115*, 20018−20026.

(44) Key, B.; Bhattacharyya, R.; Morcrette, M.; Seznéc, V.; Tarascon, J.-M.; Grey, C. P. Real-Time NMR Investigations of Structural Changes in Silicon Electrodes for Lithium-Ion Batteries. *J. Am. Chem. Soc.* **2009**, *131*, 9239−9249.

(45) Key, B.; Morcrette, M.; Tarascon, J.-M.; Grey, C. P. Pair Distribution Function Analysis and Solid State NMR Studies of Silicon Electrodes for Lithium Ion Batteries: Understanding the (De)Lithiation Mechanisms. *J. Am. Chem. Soc.* **2011**, *133*, 503−512.

(46) Artrith, N.; Urban, A.; Wang, Y.; Ceder, G. Atomic-Scale Factors That Control the Rate Capability of Nanostructured Amorphous Si for High-Energy-Density Batteries. Jan 26, 2019, arXiv:1901.09272v1 [cond-mat.dis-nn]. https://arxiv.org/abs/1901.09272 (accessed June 22, 2022).